Steep Cosmic-Ray Spectra with Revised Diffusive Shock Acceleration

Rebecca Diesing[1] and Damiano Caprioli[1,2]

[1] Department of Astronomy and Astrophysics, The University of Chicago, 5640 South Ellis Avenue, Chicago, IL 60637, USA; rrdiesing@uchicago.edu
[2] Enrico Fermi Institute, The University of Chicago, Chicago, IL 60637, USA

Abstract

Galactic cosmic rays (CRs) are accelerated at the forward shocks of supernova remnants (SNRs) via diffusive shock acceleration (DSA), an efficient acceleration mechanism that predicts power-law energy distributions of CRs. However, observations of nonthermal SNR emission imply CR energy distributions that are generally steeper than E^{-2}, the standard DSA prediction. Recent results from kinetic hybrid simulations suggest that such steep spectra may arise from the drift of magnetic structures with respect to the thermal plasma downstream of the shock. Using a semi-analytic model of nonlinear DSA, we investigate the implications that these results have on the phenomenology of a wide range of SNRs. By accounting for the motion of magnetic structures in the downstream, we produce CR energy distributions that are substantially steeper than E^{-2} and consistent with observations. Our formalism reproduces both modestly steep spectra of Galactic SNRs ($\propto E^{-2.2}$) and the very steep spectra of young radio supernovae ($\propto E^{-3}$).

Unified Astronomy Thesaurus concepts: Galactic cosmic rays (567); Shocks (2086); Supernova remnants (1667); Cosmic rays (329); Spectral index (1553); High energy astrophysics (739)

1. Introduction

Understanding the origin of Galactic cosmic rays (CRs) with energies up to $\sim 10^8$ GeV requires a complete paradigm for their acceleration and propagation. The best source candidates for such acceleration are supernova remnants (SNRs), which provide sufficient energy and an efficient acceleration mechanism (Hillas 2005; Berezhko & Völk 2007; Ptuskin et al. 2010; Caprioli et al. 2010a). In this mechanism, known as *diffusive shock acceleration* (DSA), particles are scattered by magnetic field perturbations, resulting in diffusion across the SNR forward shock and an energy gain with each crossing (Fermi 1954; Axford et al. 1977; Krymskii 1977; Bell 1978; Blandford & Ostriker 1978).

DSA predicts a power-law momentum distribution of particles, $f_{sh}(p) \propto p^{-q_p}$, where $f_{sh}(p)$ is the instantaneous momentum distribution of particles at the shock and q_p is set by the balance between the energy gained with each crossing and the escape of particles from the acceleration region (Bell 1978). Both of these quantities depend on the shock hydrodynamics such that q_p can be written in terms of the fluid compression ratio, $R = \rho_2/\rho_0$. Here, ρ_1 and ρ_2 are the densities of the fluid in front of the shock (upstream) and behind the shock (downstream) respectively. The relationship between q_p and R reads,

$$q_p = \frac{3R}{R-1}. \tag{1}$$

For a strong shock with Mach number $M \gg 1$, $R = 4$ and we obtain $q_p = 4$. Equivalently, DSA predicts power-law distributions in energy for relativistic particles, $\Phi_{sh}(E) \propto E^{-q}$, where $\Phi_{sh}(E)$ is the instantaneous energy distribution of particles at the shock. The relationship between q and R reads as

$$q = \frac{R+2}{R-1}, \tag{2}$$

with $q = 2$ for a strong shock ($R = 4$).

A modification to the standard DSA prediction arises when CRs carry a non-negligible fraction of the shock's energy. When this occurs, CRs can no longer be treated as test particles, resulting in modifications to the shock hydrodynamics and thus particle spectra (e.g., O'C. Drury & Völk 1981; O'C. Drury 1983; Blandford & Eichler 1987; Jones & Ellison 1991; Berezhko & Völk 1997; Malkov & O'C. Drury 2001; Kang & Jones 2005, 2006; Ellison et al. 2000, 1996; Berezhko & Ellison 1999; Amato & Blasi 2005, 2006; Caprioli et al. 2009b, 2008). In this nonlinear DSA (NLDSA), the CR pressure produces a region in front of the shock where the fluid is compressed, heated, and slowed. The presence of this region, or *precursor*, reduces the compression ratio near the shock into a subshock with $R_{sub} \equiv \rho_2/\rho_1 < 4$. Meanwhile, the total compression ratio between the downstream and far upstream becomes larger than the standard prediction: $R_{tot} \equiv \rho_2/\rho_0 > 4$. Note that, throughout this paper, subscripts 0, 1, 2, and 3 are used to denote quantities at upstream infinity, immediately upstream of the shock, immediately downstream of the shock, and far downstream, respectively (see Figure 1).

As a result of these two compression ratios, NLDSA predicts concave CR spectra. More specifically, particles with lower energies remain close to the shock and probe $R_{sub} < 4$, while particles with higher energies diffuse further upstream and probe $R_{tot} > 4$. Thus, low/high-energy particles are expected to exhibit spectra steeper/flatter than E^{-2}. The transition between these regimes occurs at the lowest energy where CRs carry non-negligible pressure, which is usually trans-relativistic. Since the nonthermal emission in astrophysical environments is typically generated by relativistic CRs, the classical NLDSA theory predicts that observations of nonthermal emission from shock-powered sources should be explained by CR spectra flatter than E^{-2}.

1.1. Theory versus Observations

This prediction is readily testable via observations of the nonthermal emission, e.g., from the relics of stellar explosions.
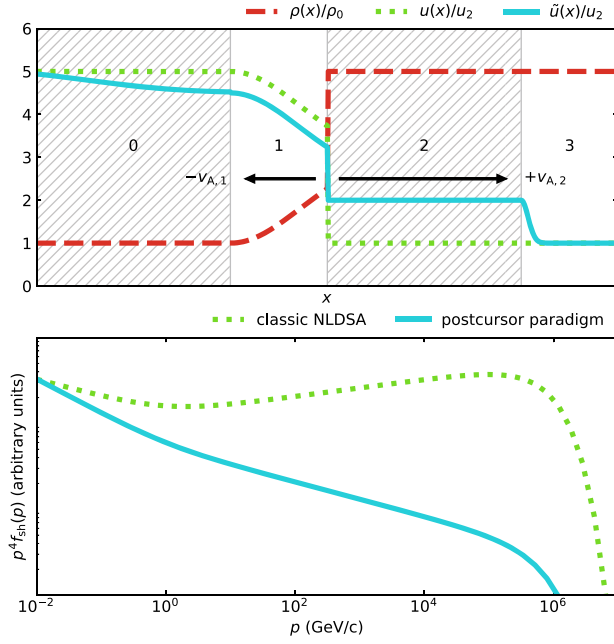
Figure 1. *Top*: a sketch of the fluid density ($\rho(x)$; red dashed line), fluid velocity ($u(x)$; green dotted line), and the velocity of magnetic fluctuations ($\tilde{u}(x) = u(x) + v_A(x)$; blue solid line) for a CR-modified shock with precursor (Region 1) and postcursor (Region 2). Velocities are displayed in the shock rest frame. *Bottom*: a sketch of the expected instantaneous particle distribution, $f_{\rm sh}(p)$, in the case with no net drift of magnetic fluctuations (classic NLDSA; green dotted line) and in the case with the net drifts shown in the top figure (postcursor paradigm; blue solid line). In the postcursor paradigm, particles experience an effective compression ratio smaller than that of the fluid, resulting in steeper spectra.

However, the first gigaelectronvolt (GeV) observations of SNRs, combined with preexisting teraelectronvolt (TeV) data, did not confirm the existence of concave spectra. On the contrary, they pointed toward CR acceleration with spectra *steeper* than E^{-2} (Caprioli 2011). Notable examples include historical remnants such as Tycho's SNR ($q = 2.3 \pm 0.2$, Giordano et al. 2012; Archambault et al. 2017) and Cassiopeia A ($q = 2.36 \pm 0.02$ above 17 GeV, Saha et al. 2014).

Further evidence for steep spectra comes in the form of SNR radio emission, particularly that of young, extragalactic supernovae (*radio SNe*). These remnants exhibit synchrotron spectra that imply electron distributions as steep as E^{-3} (e.g., Chevalier & Fransson 2006, 2017; Soderberg et al. 2010, 2012; Kamble et al. 2016). However, it is possible that these synchrotron spectra probe the steep portion of a concave spectrum, since the electrons responsible are likely sub-gigaelectronvolt (e.g., Ellison & Reynolds 1991; Ellison et al. 2000; Tatischeff 2009).

The CR spectrum measured at Earth also points toward CR acceleration with spectra steeper than E^{-2}. In the standard picture of CR transport, this measured CR spectrum goes as $E^{-(q+\delta)}$, where δ is the slope of the CR residence time in the Galaxy: $\tau_{\rm res} \propto E^{-\delta}$. Measurements of the CR anisotropy suggest $\delta \sim 0.3$ (Blasi & Amato 2012a, 2012b). Meanwhile, secondary to primary ratios suggest that $0.3 \lesssim \delta \lesssim 0.4$, depending on the CR energy (e.g., AMS Collaboration et al. 2018). Thus, fitting the observed Galactic CR spectrum—which goes as $E^{-2.7}$–requires $2.3 \lesssim q \lesssim 2.4$ (Evoli et al. 2019, 2020).

1.2. A Revised Theory of DSA

A number of explanations for steep CR spectra have been proposed in the literature. These explanations include the following:

1. Anisotropic or inhomogeneous CR transport (e.g., Kirk et al. 1996; Bell et al. 2011, and references therein) at fast oblique shocks ($v_{\rm sh} \gtrsim 10^4$ km s^{-1}). While such transport could explain the steep spectra of radio SNe, it does not apply to quasi-parallel and/or slower shocks (i.e., older SNRs).

2. Modified shock dynamics due to the presence of neutral hydrogen (Blasi et al. 2012; Morlino et al. 2012, 2013) and/or steepening due to ion-neutral damping (Malkov et al. 2012). While this idea may be consistent with the steep spectra of some SNRs propagating into a partially ionized medium (e.g., Morlino & Blasi 2016), it cannot explain radio SNe, since for fast shocks ($v_{\rm sh} \gtrsim 3000$ km s^{-1}), ionization becomes dominant thereby eliminating the neutral return flux. Moreover, it is unclear whether ion-neutral damping would produce a steepening or a low-energy cutoff around a few GeV that would effectively halt the acceleration process.

3. Effects arising from the convolution of multiple CR distributions, either over time (Malkov & Aharonian 2019), or space, specifically the convolution of spectra from regions in which the large scale magnetic field is either quasi-parallel or quasi-perpendicular to the shock normal (Hanusch et al. 2019). However, both effects may only work with the inclusion of ad hoc shock obliquities. Moreover, the former effect is predicated on a growing region in which the shock is quasi-parallel, and therefore cannot explain SNRs with magnetic field coherence lengths that are smaller than the size of the system (e.g., Tycho). The latter would not apply in SNRs that probe a uniform background magnetic field (e.g., SN 1006).

4. CR energy loss in the upstream due to the generation of magnetic turbulence (Bell et al. 2019). While such an effect may in principle steepen DSA spectra, it is not observed in kinetic simulations, as outlined in more detail below.

A more detailed summary of these explanations and their limitations can be found in Caprioli et al. (2020).

Another possible explanation considers the role of the magnetic fluctuations responsible for CR scattering (e.g., Zirakashvili & Ptuskin 2008; Caprioli 2011, 2012; Kang & Ryu 2018). In the standard DSA theory, particles are isotropized in both the upstream and downstream such that they *feel* a head–on collision with each crossing of the shock. The resulting energy gain per crossing thus depends on the difference in velocity between the upstream and downstream plasma, $u_1 - u_2$. In reality, however, magnetic fluctuations—not thermal plasma—are responsible for particle scattering, meaning that particles will be isotropized in the *fluctuation* frame. The relative drift between the fluid and the fluctuations was already present in the early DSA theory (Bell 1978), but it has been usually neglected because the fluctuation drift is roughly the Alfvén speed, much smaller than the fluid speed in the shock frame. In the presence of CR-driven magnetic field amplification, however, such a drift may be significantly enhanced; one could argue that, in the upstream, these fluctuations move against the fluid with the local Alfvén velocity

in the amplified field, $v_{A,1}$ (e.g., Caprioli 2012). Thus, CRs experience a smaller energy gain per crossing $\propto u_1 - v_{A,1} - u_2$, or equivalently, they *feel* a compression ratio, $\tilde{R}$ that is smaller than that of the fluid,

$$\tilde{R} = \frac{u_1 - v_{A,1}}{u_2} < R = \frac{u_1}{u_2}. \qquad (3)$$

This prescription may naturally lead to spectra that are steeper than E^{-2} (Caprioli 2011, 2012), and it has been used, e.g., to model for the broadband emission of Tycho's SNR (Morlino & Caprioli 2012; Slane et al. 2014) and of intracluster shocks (Kang et al. 2013).

The potential role of such drifts had not been validated by self-consistent kinetic simulations until very recently, when Haggerty & Caprioli (2020) and Caprioli et al. (2020) put forward unprecedentedly long hybrid simulations (i.e., particle-in-cell simulations with kinetic ions and fluid electrons) that showed the onset of CR-modified shocks. That being said, the presence of a precursor is insufficient to explain the very steep spectra ($\propto E^{-3}$) of radio SNe, and its effect may be limited if magnetic field amplification in the upstream is spatially dependent. In particular, if the local Alfvén speed decreases in the precursor, particles with long diffusion lengths will probe a region with reduced fluctuation drift, resulting in a flattening of the CR spectrum at the highest energies.

However, Haggerty & Caprioli (2020) find that not only does a precursor form in front of the shock, in which self-generated fluctuations move at roughly $v_{A,1}$ in the amplified field, but also that the motion of magnetic structures behind the shock leads to the formation of a *postcursor*. In this picture, CR-driven magnetic fluctuations generated in the upstream retain their inertia over a non-negligible distance (larger than the CR diffusion length) when advected and compressed into the downstream. As a result, these fluctuations move away from the shock faster than the background plasma, or more specifically, with velocity $\tilde{u}_2 = u_2 + v_{A,2}$ with respect to the shock. A sketch of a CR-modified shock, with precursor and postcursor included, is shown in Figure 1.

Since CRs tend to isotropize with magnetic fluctuations, they too experience a net drift equal to $v_{A,2}$ relative to the background plasma (see Figure 6 in Haggerty & Caprioli 2020). These drifts away from the shock lead to the removal of CR and magnetic energy from the shock and thus an enhancement of the fluid compression ratio and a steepening of the CR spectrum, as discussed in Section 5 of Haggerty & Caprioli (2020).

Equivalently, one can think of the postcursor as modifying the compression ratio *felt* by CRs, just as the precursor modifies this ratio in Caprioli (2012). In the postcursor paradigm (ignoring, for now, the presence of a precursor), we have,

$$\tilde{R} = \frac{u_1}{u_2 + v_{A,2}} = \frac{R}{1 + \alpha}, \qquad (4)$$

where $\alpha \equiv v_{A,2}/u_2$. Thus, q_p depends only on R and α, or equivalently, on R and the magnetic pressure fraction downstream, $\xi_{B,2} \equiv B_2^2/(8\pi\rho_0 v_{sh}^2)$:

$$q_p = \frac{3R}{R - 1 - \alpha} = \frac{3R}{R - 1 - \sqrt{2R\xi_{B,2}}}. \qquad (5)$$

Note that the effect of the postcursor will dominate that of a precursor, since compression of the magnetic field in the downstream leads to $\alpha > v_{A,1}/u_1$ (Caprioli et al. 2020). In the case of efficient CR acceleration and thus magnetic field amplification, Haggerty & Caprioli (2020) report $\alpha \sim 0.6$, which is sufficient to produce spectra steeper than p^{-4}, or E^{-2} at relativistic energies.

While these hybrid simulations provide a motivation and a physical explanation for the modification of the standard DSA theory, quantifying the steepening of the CR spectra in astrophysical systems requires additional calculations. Namely, the postcursor paradigm implies that spectral steepening increases with the downstream magnetic field strength, which, due to magnetic field amplification via CR-driven instabilities, increases with the CR pressure (e.g., Bell 2004; Cristofari et al. 2021). However, if spectra become too steep, the CR pressure will drop, reducing magnetic field amplification and thus causing the steepening to saturate.

In this paper, we use a semi-analytic model of NLDSA to generalize the results of Caprioli et al. (2020) and estimate q for a wide range of SNR shocks. We describe this model in detail in Section 2. In Sections 3 and 4, we present the results of our calculations and find that our modeled spectra produce good agreement with observations of both Galactic SNRs and radio SNe. We summarize in Section 5.

2. Method

To fully understand how a postcursor affects CR acceleration, we use a semi-analytic formalism to model SNR shocks over a range of ambient number densities, n_{ISM}, ambient magnetic fields, B_0, and SN energies, E_{SN}. Herein we describe this formalism briefly, including our models for SNR evolution, particle acceleration, and magnetic field amplification. A more detailed description of our model, particularly our prescription for particle acceleration, can be found in Caprioli (2012) and Diesing & Caprioli (2019).

2.1. Shock Hydrodynamics

We model SNR shock hydrodynamics using the formalism described in Diesing & Caprioli (2018), which includes the effect of CR pressure on the evolution of the shock. More specifically, SNR evolution is modeled through three stages spanning $\gtrsim 10^5$ yr: the *ejecta-dominated stage*, in which the mass of the swept-up ambient gas is less than that of the SN ejecta, the *Sedov stage*, in which the swept-up mass dominates the total mass and the SNR expands adiabatically, and the *pressure-driven snowplow*, in which the remnant cools due to forbidden atomic transitions but continues to expand because its internal pressure exceeds the ambient pressure. After this point, the remnant enters the *momentum-driven snowplow*, in which the internal pressure falls below the ambient pressure and expansion continues due to momentum conservation.

While we model SNRs through the end of the pressure-driven snowplow, the majority of CRs are accelerated during the transition between the ejecta-dominated and Sedov stages. The DSA timescale for CRs of energy $E = E_{max}$ is given by $\tau_{DSA} \approx D/v_{sh}^2$ where D is the diffusion coefficient and v_{sh} is the shock speed. Assuming Bohm diffusion (Caprioli & Spitkovsky 2014a), $D(E) \propto r_L \propto E/B_2$, where r_L is the Larmor radius and B_2 is the post-shock magnetic field. This gives $E_{max} \propto B_2 v_{sh}^2 t$, and since v_{sh} is roughly constant during the

ejecta-dominated stage, $E_{\max}$ initially increases. After the transition to the Sedov stage, the shock slows down such that $v_{\mathrm{sh}} \propto t^{-3/5}$, meaning that $E_{\max}$ decreases with time, i.e., $E_{\max} \propto B_2(t) t^{-1/5}$ (Cardillo et al. 2015; Bell et al. 2013). The spectra of middle-aged and old SNRs are therefore most sensitive to shock evolution during the early adiabatic stages.

All SNRs are assumed to eject $M_{\mathrm{ej}} = 1\,M_{\odot}$ (1 solar mass) with $E_{\mathrm{SN}} \in [10^{51},\ 10^{52}]$ erg into a uniform ambient medium of density $n_{\mathrm{ISM}} \in [10^{-1},\ 10^{5}]\,\mathrm{cm}^{-3}$ and magnetic field $B_0 \in [3,\ 3000]\,\mu\mathrm{G}$.

2.2. Particle Acceleration

We model CR acceleration using the semi-analytic model of NLDSA described in Caprioli et al. (2009b, 2010b), Caprioli (2012), Diesing & Caprioli (2019), and references therein, in particular Malkov (1997), Malkov et al. (2000), Blasi (2002, 2004), and Amato & Blasi (2005, 2006). This model self-consistently solves the diffusion-advection equation for the transport of nonthermal particles in a quasi-parallel, nonrelativistic shock, including the dynamical backreaction of accelerated particles and of CR-generated magnetic turbulence.

Particles above a threshold in momentum, p_{inj}, are injected into the acceleration process, with $p_{\mathrm{inj}} \equiv \xi_{\mathrm{inj}} m_{\mathrm{p}} v_{\mathrm{sh}} / (1 + R_{\mathrm{tot}}^{-1})$, consistent with the parameterization described in Caprioli et al. (2015), since $v_{\mathrm{sh}} / (1 + R_{\mathrm{tot}}^{-1})$ is simply the velocity of the upstream fluid in the downstream frame. In general, an increase in ξ_{inj} corresponds to a decrease in the fraction of particles crossing the shock that are injected into DSA. Here, we neglect the dependence of injection on the shock inclination and set an effective value of $\xi_{\mathrm{inj}} = 3.8$, which yields $\xi_{\mathrm{CR}} \equiv P_{\mathrm{CR}} / (\rho_0 v_{\mathrm{sh}}^2) \approx 0.1$ for a prototypical SNR ($n_{\mathrm{ISM}} = 1\,\mathrm{cm}^{-3}$, $B_0 = 3\,\mu\mathrm{G}$, $E_{\mathrm{SN}} = 10^{51}$ erg, and $M_{\mathrm{ej}} = 1 M_{\odot}$) after a few hundred years, consistent with SNR observations. Note that P_{CR} refers to the CR pressure.

To account for the effects of a precursor and postcursor, we introduce into the diffusion-advection equation $\tilde{u}(x) \equiv u(x) \pm v_{\mathrm{A}}(x)$, the effective fluid velocity as felt by the nonthermal particles, which are scattered by magnetic structures moving at $v_{\mathrm{A}}(x)$ relative to the thermal plasma. Note that these structures move *against* the fluid in the upstream, but *with* the fluid in the downstream (Caprioli et al. 2020). Throughout this work, we assume that the postcursor extends beyond the diffusion length of the highest energy particles, i.e., behind the shock, $\tilde{u}(x) = u_2 + v_{\mathrm{A},2}$.

The actual extent of the postcursor in astrophysical shocks is difficult to quantify, even if high-resolution X-ray observations of individual SNRs with Chandra suggest that the magnetic field remains amplified on a scale of 1%–5% of the SNR radius (e.g., Tran et al. 2015). Physically speaking, since the maximum CR energy $E_{\max}$ is controlled by the smallest between the upstream and the downstream diffusion lengths (e.g., O'C. Drury 1983; Lagage & Cesarsky 1983a; Blasi et al. 2007), the post-shock region with high magnetic field must be at least as extended as the diffusion length of particles with $E_{\max}$. It follows that the postcursor must be more extended than the diffusion length of any particle, thereby leading to a *global* steepening of the CR spectrum. Note that when only the Alfvénic drift in the precursor is retained (á la Zirakashvili & Ptuskin 2008; Caprioli 2012), a global steepening is only possible if escaping CRs drive magnetic field amplification on all scales, which is not guaranteed.

In practice, our formalism begins with an initial guess for the CR pressure, which is used to solve the equations for conservation of mass, momentum, and energy across a plane, nonrelativistic shock. The magnetic field pressure, P_{B}, is then calculated using the prescription described in Section 2.3, and the resulting $u(x)$ and P_{B} are then used to solve the diffusion-advection equation, which can be integrated to find a new guess for P_{CR}. In this manner, our formalism iteratively solves for the CR spectrum while self-consistently accounting for the dynamical effect of accelerated particles and the amplification of magnetic fields.

Once the proton spectrum has been calculated at each time step of SNR evolution, particle momenta are shifted and the instantaneous spectra are weighted to account for adiabatic losses (see Caprioli et al. 2010a; Morlino & Caprioli 2012; Diesing & Caprioli 2019, for more details). These weighted contributions are then added together to obtain a cumulative spectrum.

2.3. Magnetic Field Amplification

The propagation of energetic particles ahead of the shock is expected to excite streaming instabilities, (Bell 1978, 2004; Amato & Blasi 2009; Bykov et al. 2013), which drive magnetic field amplification and enhance CR diffusion (Caprioli & Spitkovsky 2014b, 2014a). The result is magnetic field perturbations with magnitudes that can exceed that of the ordered background magnetic field. This magnetic field amplification has been observationally inferred from the X-ray emission of many young SNRs, which exhibit narrow X-ray rims due to synchrotron losses by relativistic electrons (e.g., Bamba et al. 2005; Parizot et al. 2006; Morlino et al. 2010; Ressler et al. 2014).

We model magnetic field amplification by assuming contributions from both the resonant streaming instability (e.g., Kulsrud & Pearce 1968; Zweibel 1979; Skilling 1975a, 1975b, 1975c; Bell 1978; Lagage & Cesarsky 1983a), and the nonresonant hybrid instability (Bell 2004). A detailed discussion of these instabilities and their saturation points can be found in Cristofari et al. (2021).

In the resonant instability, CRs excite Alfvén waves with a wavelength matching their gyroradius. The growth of this instability saturates when the strength of magnetic perturbations reaches the level of the ordered background field: $\delta B / B \sim 1$. More specifically, Amato & Blasi (2006) derive this saturation level to be

$$P_{\mathrm{B1,res}} = \frac{P_{\mathrm{CR},1}}{4 M_{\mathrm{A},0}}, \tag{6}$$

where $M_{\mathrm{A}} \equiv v_{\mathrm{sh}} / v_{\mathrm{A},0}$ is the Alfvénic Mach number.

For fast shocks typical of young SNRs, more significant is the nonresonant hybrid instability. Driven by CR currents, $\boldsymbol{j}$, in the upstream, Bell (2004) predicts that saturation occurs when tension in magnetic field lines becomes sufficient to oppose the $\boldsymbol{j} \times \boldsymbol{B}$ force, or equivalently, when the magnetic field pressure reaches approximate equipartition with the anisotropic fraction of the CR pressure (also see Blasi et al. 2015),

$$P_{\mathrm{B1,Bell}} = \frac{v_{\mathrm{sh}}}{2c} \frac{P_{\mathrm{CR},1}}{\gamma_{\mathrm{CR}} - 1}. \tag{7}$$
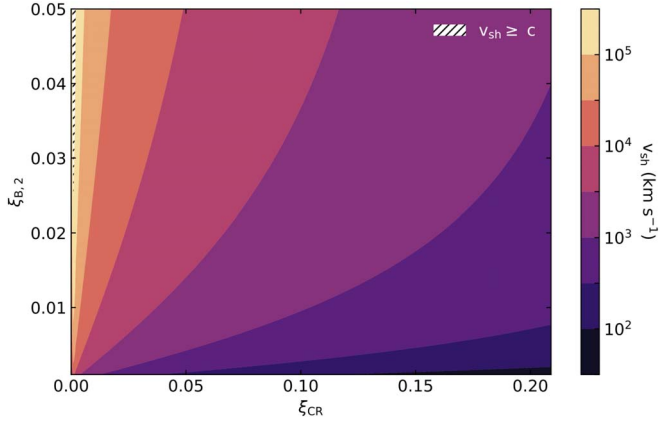
Figure 2. Shock velocity, denoted by color scale, as a function of CR acceleration efficiency, ξ_{CR}, and magnetic pressure fraction downstream, $\xi_{B,2}$, assuming a strong shock and magnetic field amplification dominated by the nonresonant streaming instability. Note that faster shocks correspond to stronger downstream magnetic fields given a fixed ξ_{CR}.
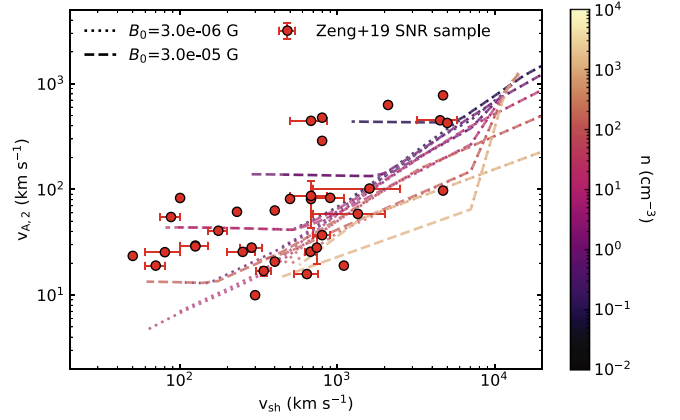

Figure 3. Downstream Alfvén speed, $v_{A,2}$, as a function of shock velocity, v_{sh} for a number of modeled SNR evolutions (dotted and dashed lines). Each line corresponds to a single evolution with a fixed ambient density (color scale) and ambient magnetic field (line style). Overlaid are the SNR data aggregated in Zeng et al. (2019). Our prescription for magnetic field amplification produces modeled SNRs in good agreement with the measured relationship between $v_{A,2}$ and v_{sh}.

Here, c is the speed of light and $\gamma_{CR} = 4/3$ is the CR adiabatic index. This saturation can lead to $\delta B/B_0 \gg 1$ and has been validated with hybrid simulations in Zacharegkas et al. (2019). Thus, if the nonresonant instability dominates magnetic field amplification, one can solve the equations for conservation of mass, momentum, and energy across the shock to obtain a compression ratio (see the Appendix), yielding a well-defined relationship between the shock velocity, the CR acceleration efficiency (ξ_{CR}), and the magnetic pressure faction downstream, ($\xi_{B,2}$). This relationship is shown in Figure 2 for a reasonable range of ξ_{CR} and $\xi_{B,2}$.

To account for both the resonant and nonresonant instabilities, we pose here that the upstream magnetic field pressure is given by $P_{B,1} = \sqrt{P_{B1,res}^2 + P_{B1,Bell}^2}$. The nonresonant instability dominates provided that $v_{sh} > v_{sh}^*$, where v_{sh}^* is derived from the condition that $P_{B1,res} = P_{B1,Bell}$ and is given by

$$v_{sh}^* = \sqrt{\frac{v_{A,0}c}{6}} \simeq 572 \text{ km s}^{-1} \left(\frac{B_0}{3\mu G}\right)^{1/2} \left(\frac{n_0}{\text{cm}^{-3}}\right)^{-1/4}. \quad (8)$$

$v_{sh}^*(n_0, B_0)$ is denoted by vertical lines in Figure 6. Assuming that all components of the magnetic perturbations upstream are compressed, the downstream magnetic field strength is $B_2 \simeq R_{sub}B_1$.

Note that a comprehensive theory for magnetic field amplification upstream of a shock is still missing. In particular, the relative contribution of escaping CRs (e.g., Vladimirov et al. 2006; Caprioli et al. 2009a; Bell et al. 2013) and diffusing CRs (e.g., Bell 2004; Amato & Blasi 2006) may depend on their spectral slope. The actual value of the field in the postcursor should, in principle, depend in a nonlinear way on the steepening that it induces (see Cristofari et al. 2021, for an extended discussion of these effects). Such a self-regulating backreaction is not accounted for in the present calculation, but we check a posteriori that our prescription for magnetic field amplification is consistent with observations.

For an acceleration efficiency $\xi_{CR} \approx 0.1$, our typical SNR parameters give B_2 near a few hundred microgauss, in good agreement with X-ray observations of young SNRs (Völk et al. 2005; Parizot et al. 2006; Caprioli et al. 2008).

For a more robust test of our prescription, we consider the relationship between v_{sh} and $v_{A,2}$. Specifically, our prescription predicts a positive relationship between v_{sh} and $v_{A,2}$ for large v_{sh} (i.e., where the nonresonant instability dominates). This relationship is independent of the ambient density, and for a strong shock with a weak precursor (i.e., $R_{sub} = R_{tot} = 4$) reads

$$v_{A,2} \simeq 40 \, k \text{ ms}^{-1} \left(\frac{v_{sh}}{1000 \, k \text{ ms}^{-1}}\right)^{3/2} \left(\frac{\xi_{CR}}{0.1}\right)^{1/2}. \quad (9)$$

At lower v_{sh} (i.e., where the resonant instability dominates), we would expect little to no correlation, since the resonant instability has a weaker dependence on v_{sh} and depends on the ambient magnetic field, which may vary. In Figure 3, we compare our predicted relationship between $v_{A,2}$ and v_{sh} to observational results compiled in Zeng et al. (2019). As Figure 3 shows, our prescription yields a good agreement with observations. This agreement also provides circumstantial evidence that the presence of a postcursor is responsible for steep SNR spectra, particularly in light of the fact that SNRs with large v_{sh} tend to have larger q (e.g., Bell et al. 2011).

3. Results

Herein we present our modeled CR spectra and quantify the steepening resulting from the modified shock dynamics—namely, the presence of a postcursor described in Haggerty & Caprioli (2020) and Caprioli et al. (2020). Throughout this and subsequent sections, we estimate power-law slopes as

$$q \equiv -\left\langle \frac{d \log \Phi(E)}{d \log E}\right\rangle, \quad (10)$$

where $\Phi(E) = dN(E)/dE$ is the cumulative proton spectrum and q is averaged between 10 and 10^3 GeV.
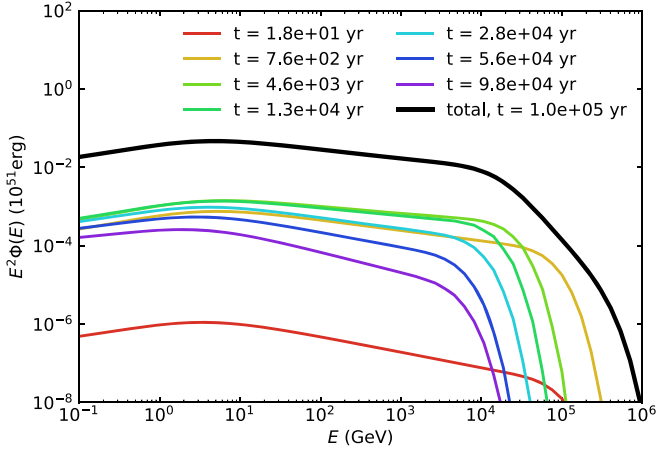
Figure 4. The modeled proton distribution, $\Phi(E)$, for a Tycho-like SNR: $n_{\text{ISM}} = 1$ cm^{-3}, $B_0 = 3$ μG, $E_{\text{SN}} = 10^{51}$ erg, and $M_{\text{ej}} = 1M_\odot$. The black line shows the cumulative proton spectrum after 10^5 yr, while the colored lines show the contributions to this final spectrum from various time steps. Throughout the SNR's evolution, protons are accelerated with spectra steeper than E^{-2}.

3.1. SNR Spectra

Our modeled spectrum of a *prototypical*, or Tycho-like SNR ($n_{\text{ISM}} = 1$ cm^{-3}, $B_0 = 3$ μG, $E_{\text{SN}} = 10^{51}$ erg, and $M_{\text{ej}} = 1M_\odot$) is shown in Figure 4, including the contributions of protons accelerated at various stages of its evolution. These contributions are all steeper than E^{-2}, resulting in a cumulative spectrum $\Phi(E) \propto E^{-2.23}$ by the end of the SNR lifetime ($\sim 10^5$ yr).

It is also worth noting that the slopes of these contributions do not vary monotonically. For the first $\sim 10^4$ yr, steepening due to the postcursor becomes less pronounced as the shock decelerates and the downstream magnetic field decreases (recall that $P_{\text{B1,Bell}} \propto v_{\text{sh}} P_{\text{CR}} \propto v_{\text{sh}}^3$, assuming the acceleration efficiency, ξ_{CR} remains constant). After this point, v_{sh} approaches a few hundred kilometers per second and the resonant streaming instability becomes the dominant source of magnetic field amplification. This instability has a weaker dependence on v_{sh}: $P_{\text{B1,res}} \propto P_{\text{CR}}/M_{\text{A,0}} \propto v_{\text{sh}}$, again assuming constant ξ_{CR}. As a result, the spectrum stops hardening and actually begins to steepen slightly as ξ_{CR} drops and the fluid compression ratio decreases. Note that, in our model, the drop in ξ_{CR} is due to a decline of the post-shock temperature and the ensuing decrease in the injection momentum ($p_{\text{inj}} \propto v_{\text{sh}}$), resulting in fewer of the petaelectronvolt particles that are largely responsible for the CR pressure.

The variation in the CR slope in conjunction with the decrease with time of E_{max} yields a cumulative proton distribution with a high-energy tail that is more extended than a simple exponential cutoff. Note that, with our prescription, this high-energy tail does not make it to GeV energies, or the *knee* of the CR spectrum. This issue may be resolved by invoking a different class of SNR (see, e.g., Bell et al. 2013; Cardillo et al. 2015; Cristofari et al. 2021).

3.2. Spectral Steepening

A more explicit quantification of the effect of the postcursor can be found in Figure 5. Here, we compare the cumulative spectrum of our Tycho-like SNR after 400 yr to the traditional NLDSA result and to the case with a postcursor but no net motion of magnetic structures in the precursor. As expected, the NLDSA formalism produces a modestly concave spectrum
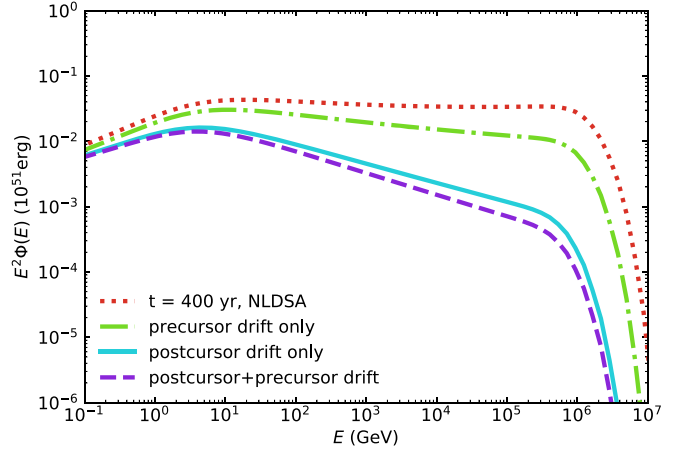

Figure 5. The modeled proton distribution of the Tycho-like SNR described in Figure 4 after 400 yr. Spectra are shown assuming traditional NLDSA with no net drift of magnetic fluctuations (red dotted line), assuming net drift in the precursor only (green dotted–dashed line), assuming net drift in the postcursor only (blue solid line), and assuming the net drift in both the precursor and postcursor (purple dashed line). The inclusion of postcursor drift produces a substantial spectral steepening relative to the traditional NLDSA prediction. The addition of precursor drift further steepens the proton spectrum, but its effect is subdominant.

that deviates slightly from the standard E^{-2} prediction. Meanwhile, the addition of a postcursor softens this spectrum substantially to $E^{-2.30}$. The addition of a precursor yields a slight increase in this steepening to $E^{-2.34}$, but its effect is underdominant due to the fact that the upstream magnetic field is decompressed such that $v_{\text{A,1}}/u_1 < v_{\text{A,2}}/u_2$.

A summary of our results can be found in Figure 6, which shows the average power-law slope, q, as a function of shock velocity, v_{sh}, for the full range of modeled SNRs described in 2.1. To span a larger velocity range, we include models with initial energy, E_{SN}, between 10^{51} and 10^{52} erg. Since increasing E_{SN} increases the shock velocity but does not otherwise affect shock hydrodynamics, we do not visually distinguish between different E_{SN} in Figure 6. A fast shock may therefore correspond to a large E_{SN} or a young SNR; from the perspective of CR acceleration and magnetic field amplification, the two scenarios are equivalent. For this reason, our parameter range effectively spans different ejecta masses as well. Namely, an increase in M_{ej} simply corresponds to a decrease in v_{sh} for a given E_{SN}. With the range of SNR parameters described in 2.1, we obtain $2.1 \lesssim q \lesssim 3$.

For large v_{sh} an increase in v_{sh} corresponds to an increase in q, as one would expect when the Bell instability drives magnetic field amplification. As suggested in Figure 4, this dependence disappears when v_{sh} becomes small enough that the resonant instability dominates, i.e., at v_{sh}^* (see Equation (8)). Thus, the dependence of v_{sh}^* on the ambient density and magnetic field introduces a spread in the relationship between q and v_{sh}, which, in the case of small ambient densities and large magnetic fields, can extend up to high v_{sh} ($\gtrsim 10^4$ km s^{-1}). More specifically, while n_{ISM} and B_0 have no significant bearing on q for $v_{\text{sh}} > v_{\text{sh}}^*$, they do determine the velocity below which q becomes roughly constant, or equivalently, the minimum value of q for a given SNR. An increase in n_{ISM} yields a modest decrease in this minimum, since $v_{\text{sh}}^* \propto n_{\text{ISM}}^{-1/4}$, while an increase in B_0 increases this minimum, since $v_{\text{sh}}^* \propto B_0^{1/2}$.
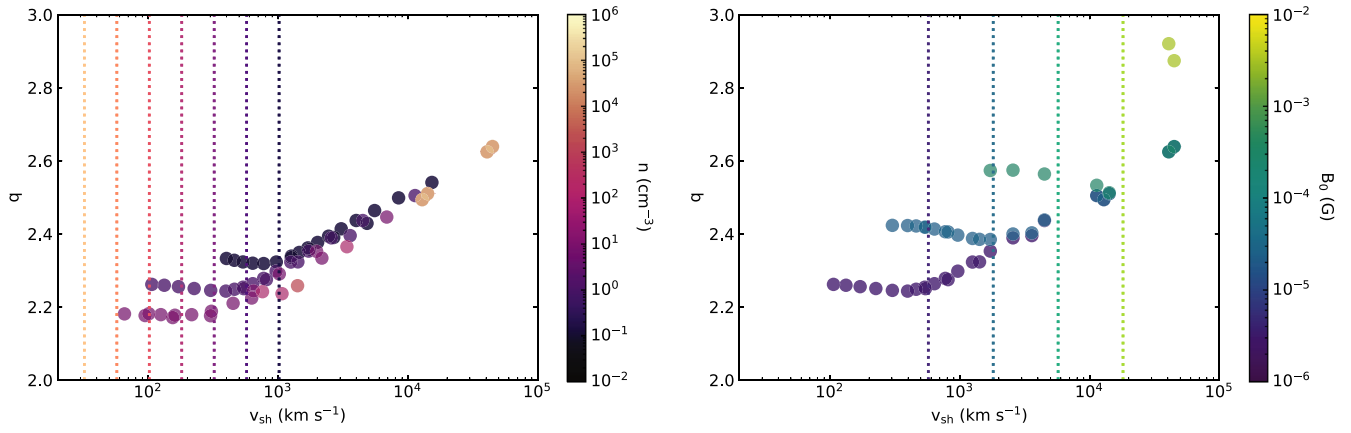
Figure 6. Power-law slopes, q, of modeled proton spectra as a function of shock velocity. The dotted vertical lines correspond to v_{sh}^*, the shock velocity where, for a given ambient density or magnetic field denoted by the color scale, the dominant source of magnetic field amplification transitions from the resonant to the nonresonant instability. *Left*: the ambient magnetic field is held fixed at 3 μG, while density, denoted by the color scale, is varied. *Right*: the ambient density is held fixed at 1 cm^{-3}, while ambient magnetic field, again denoted by the color scale, is varied. In general, faster shocks give rise to larger magnetic field amplification and thus steeper spectra. However, this dependence on shock velocity disappears at low velocities where the resonant streaming instability is the primary source of magnetic field amplification.

4. Discussion

By solving the equations for conservation of mass, momentum, and energy across a postcursor-modified shock, one can predict the fluid compression ratio as a function of the CR acceleration efficiency, ξ_{CR}, and the magnetic pressure fraction, ξ_B (see the Appendix for details). Thus, the postcursor paradigm predicts a well-defined relationship between q, ξ_{CR}, and ξ_B. Assuming magnetic field amplification is driven by the nonresonant instability, ξ_B can be recast in terms of ξ_{CR} and v_{sh}, meaning that observational constraints on the shock velocity and spectral slope correspond to constraints on the CR acceleration efficiency. For reference, we summarize this relationship in Figure 7, assuming CRs probe the full compression ratio from the far upstream to the downstream, i.e., assuming CRs with energies above $\sim$1 GeV. Less energetic CRs, such as those responsible for the synchrotron emission of radio SNe (Ellison & Reynolds 1991; Ellison et al. 2000; Tatischeff 2009), will probe smaller compression ratios and therefore exhibit slightly steeper spectra.

Equivalently, we can test the validity of the postcursor paradigm by comparing our predicted spectra to to observations, in particular the nonthermal emission of Galactic remnants (including historical SNRs), and young extragalactic SNe (radio SNe). We find that the inclusion of a postcursor can reproduce both the modestly steep spectra of Galactic remnants ($\propto E^{-2.2}$) and the very steep spectra of radio SNe ($\propto E^{-3}$).

4.1. Galactic Remnants

The SNRs in our Galaxy largely consist of older, slower shocks ($v_{sh} \ll 10^4$ km s^{-1}, see, e.g., Green 2019). Assuming magnetic field amplification driven by the nonresonant instability, we would therefore expect these SNRs—in the postcursor paradigm—to exhibit only modestly steep spectra.

To test this, we look to GeV observations aggregated in Caprioli (2011) from the Fermi-LAT source catalog (Acero et al. 2016). We opt not to use synchrotron observations to avoid complications arising from cooling. Namely, synchrotron losses produce a steepening of the electron spectrum that depends strongly on the strength of the amplified magnetic field (Diesing & Caprioli 2019). Meanwhile, TeV observations may
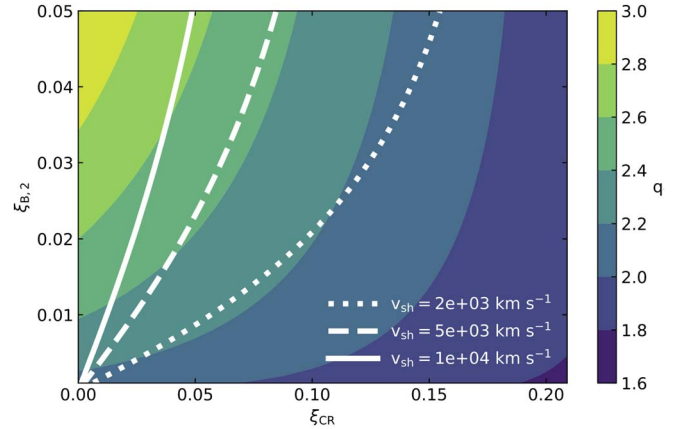

Figure 7. Predicted power-law slope, q, denoted by color scale, as a function of CR acceleration efficiency, ξ_{CR}, and magnetic pressure fraction downstream, $\xi_{B,2}$. q is calculated for a strong shock assuming CRs probe the full compression ratio from the far upstream to the downstream (regions 0 and 2, respectively; see Figure 1). White lines denoting $\xi_{B,2}$ as a function of ξ_{CR} for various shock velocities are overlaid, assuming magnetic field amplification is dominated by the nonresonant instability. As explored in Section 3, faster shocks correspond to steeper spectra for fixed ξ_{CR}.

probe the exponential cutoff of a CR distribution, artificially steepening the inferred slope. Admittedly, GeV observations suffer their own limitations. In particular, the emission process responsible for GeV photons may be π_0 decay (hadronic emission) or inverse Compton (leptonic emission). However, for Galactic remnants, it is reasonable to assume that GeV emission with a spectral energy distribution steeper than E^{-2} is hadronic in origin, since a leptonic origin would require an electron distribution steeper than E^{-3} (e.g., Ghisellini 2013). In principle, the bremsstrahlung radiation of relativistic electrons may also contribute to this GeV emission and lead to rather steep spectra, but it is usually underdominant with respect to hadronic emission for typical CR electron to proton ratios of $\lesssim$1%. We therefore remove SNRs with spectra flatter than E^{-2} for which a leptonic interpretation is favored: RX J1713.7-3946 (e.g., H.E.S.S. Collaboration et al. 2018) and Vela Jr. (e.g., Lee et al. 2013). For simplicity, we also remove SNRs with breaks
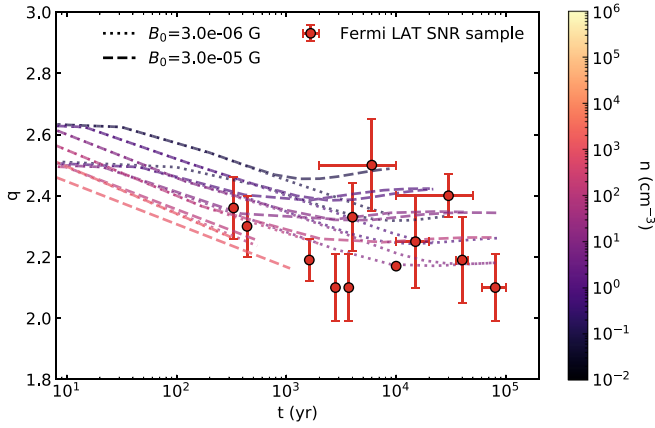
Figure 8. Power-law slopes, q, of modeled proton spectra (dotted and dashed lines) as a function of SNR age. The slopes of GeV spectra from the Fermi-LAT catalog (Acero et al. 2016) are overlaid. For simplicity, SNRs have been removed if their GeV emission is likely leptonic in origin or exhibits a significant spectral break (see text for details). The spectral information for Cassiopeia A has been taken from Saha et al. (2014). The inclusion of a postcursor produces steep proton spectra in good agreement with SNR observations.

Figure 9. The modeled proton distribution ($E^3\Phi(E)$) for a sample radio SN expanding into a circumstellar wind ($n_{\rm ISM} \propto r^{-2}$; see text for details). The black line shows the cumulative proton spectrum after 10 yr, while the colored lines show the contributions to this spectrum from various time steps. Our toy model reproduces the very steep spectra characteristic of radio SNe; for this setup, we obtain $q \simeq 2.99$.

or cutoffs in the GeV range, which are typically interpreted as due to reacceleration (e.g., W44, see Cardillo et al. 2016). When possible, we use results from combined GeV–TeV analyses (e.g., for Cas A, Saha et al. 2014), which provide a more accurate representation of the full γ-ray slope.

Figure 8 compares the values of q calculated for our modeled SNRs to those in our sample. To simplify this figure, we do not include models with $B_0 > 30 \ \mu$G, since such strong fields are more typical of radio SNe (see Section 4.2) and are not required to reproduce these observations. Furthermore, q is plotted against the estimated SNR age (t) rather than $v_{\rm sh}$. As Figure 8 shows, our models are able to reproduce the full range of slopes inferred from GeV and TeV observations of Galactic SNRs: $2.1 \lesssim q \lesssim 2.6$.

4.2. Radio SNe

In addition to explaining the modestly steep spectra of Galactic SNRs, the presence of a postcursor may also explain the very steep spectra of their extragalactic counterparts: radio SNe. These young, fast remnants ($v_{\rm sh} \gtrsim 10^4$ km s^{-1}) typically expand into dense circumstellar winds blown by the progenitor star (see, e.g., Chevalier & Fransson 2017). Their high $v_{\rm sh}$, and more explicitly, their large inferred post-shock magnetic fields (~ 0.1–1 G, see, e.g., Chevalier 1998) imply strong magnetic field amplification, making them excellent candidates for tests of postcursor physics.

Intriguingly, radio SNe exhibit synchrotron emission that suggest electron distributions $\Phi(E) \propto E^{-3}$ or even steeper (see, e.g., Chevalier & Fransson 2006; Soderberg et al. 2010, 2012; Kamble et al. 2016). Assuming protons and electrons are accelerated with the same spectral slope—a reasonable assumption given that DSA depends only on a particle's rigidity—and that synchrotron cooling is negligible at energies corresponding to radio frequencies as discussed in Chevalier & Fransson (2006), we can conclude that the proton distribution must be similarly steep.

As we have already discussed in Section 3.2, postcursor physics can reproduce $q \simeq 3$ under the right conditions: specifically, when $v_{\rm sh}$ is large and the magnetic field is generated
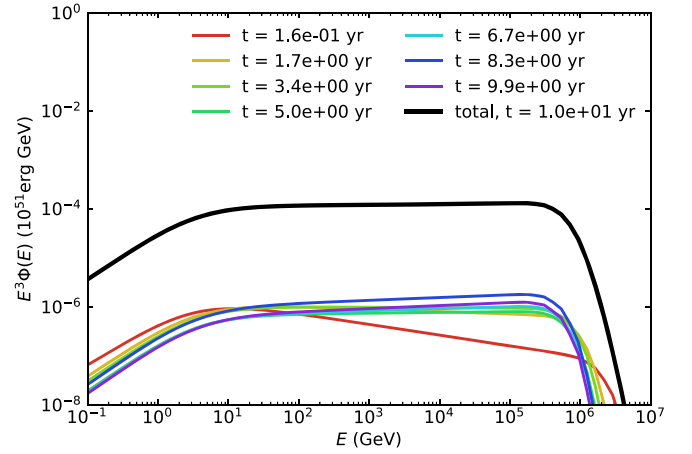
by the Bell instability. However, if our intent is to describe a typical radio SN, the models presented in 3.2 are rather rough approximations, since they assume uniform ambient densities and include an injection prescription tuned to observations of Galactic SNRs (i.e., $\xi_{\rm inj} = 3.8$ so that $\xi_{\rm CR} \approx 0.1$ for a prototypical Galactic remnant). To more accurately approximate the proton distribution of a typical radio SN, we produce a toy-model hydrodynamic evolution that follows an ejecta-dominated radio SN expanding into a circumstellar wind for approximately 10 yr. We then use our semi-analytic formalism to self-consistently calculate the corresponding proton spectrum.

More explicitly, we consider an energetic SN ($E_{\rm SN} = 10^{52}$ erg) that ejects $M_{\rm ej} = 1 \ M_\odot$ into the circumstellar medium. Since we only model the first 10 yr of evolution, the mass swept up by the shock is much smaller than $M_{\rm ej}$ and we therefore use the approximation in Table 9 of Truelove & Mc Kee (1999) for an ejecta-dominated SNR expanding into a wind: $v_{\rm sh} \propto t^{-1/5}$. For our circumstellar density, we assume a wind profile given by $\rho_0 = \dot{M}/(4\pi v_{\rm w})$, where $\dot{M}$ is the mass-loss rate of the progenitor and $v_{\rm w}$ is the wind velocity. As discussed in Chevalier & Fransson (2006), we assume typical parameters for a Wolf-Rayet progenitor: $\dot{M} = 10^{-5} M_\odot$ yr^{-1} and $v_{\rm w} = 1000$ km s^{-1}. We choose an ambient magnetic field that follows our density profile: $B_0/{\rm G} \simeq 0.01\sqrt{n_{\rm ISM}/(5000 \ {\rm cm}^{-3})}$ with normalization chosen such that our magnetic field amplification prescription produces post-shock fields consistent with observations ($B_2 \sim$ 0.1–1 G, e.g., Chevalier 1998). Finally, since $\xi_{\rm inj} = 3.8$ gives extremely small acceleration efficiencies for our toy model ($\xi_{\rm CR} < 0.01$), we reduce $\xi_{\rm inj}$ slightly to 3.4. With this adjustment, $\xi_{\rm CR}$ remains modest (<0.05). The decrease in $\xi_{\rm inj}$ needed to produce acceleration efficiencies of 5%–10% would yield even steeper spectra.

Our model spectrum is shown in Figure 9 and has a slope of $q \simeq 2.99$; note that to make this slope visually apparent, we plot $E^3\Phi(E)$. As time passes, each new shell of protons contributes a slightly harder spectrum due to the modest decrease in $v_{\rm sh}$, which leads to a reduction in magnetic field amplification (for the parameters discussed here, the nonresonant instability dominates). This behavior implies a simple physical explanation for the discrepancy between the very steep spectral slopes

of radio SNe and the modestly steep slopes of Galactic SNRs. Namely, as young remnants age and slow down, their post-shock magnetic fields decrease, reducing the strength of their postcursors and flattening their spectra. Of course, real radio SNe often exhibit spectra with more complex time variability, which may be attributed to circumstellar media that do not follow simple wind profiles (e.g., Margutti et al. 2019). Our aim here is simply to show that, with reasonable parameters, the inclusion of a postcursor can easily reproduce the very steep spectra characteristic of radio SNe.

Our model predicts CR spectra to be steep even at high energies, while the classical concave-spectra explanation (e.g., Ellison & Reynolds 1991; Ellison et al. 2000; Tatischeff 2009) returns rather flat spectra at TeV energies; therefore, X-ray, and possibly, γ-ray observations may be able to distinguish between models.

5. Conclusion

In summary, we use a semi-analytic model of NLDSA to quantify the CR spectral steepening in SNRs that arises from the presence of a *postcursor*, i.e., a region behind a shock in which magnetic fluctuations drift away from the shock at the local Alfvén speed with respect to the background fluid. Since CRs isotropize with these fluctuations, they too experience a net drift, leading to a removal of CR energy from the system and thus a steepening of their spectra relative to the standard DSA prediction ($\Phi(E) \propto E^{-2}$). Our model also includes the effect of a *precursor*, or region of enhanced CR density in front of the SNR shock. In this region, magnetic fluctuations move against the fluid (away from the shock) with the local Alfvén speed, leading to a further—albeit subdominant—steepening of the CR spectrum (Caprioli 2012). The formation of both a precursor and a postcursor has been validated with kinetic simulations (Haggerty & Caprioli 2020; Caprioli et al. 2020) and provides a natural explanation for the steep CR spectra inferred from observations of SNRs (e.g., Giordano et al. 2012; Saha et al. 2014; Archambault et al. 2017) and Galactic CRs, once corrected for propagation (e.g., AMS Collaboration 2018; Evoli et al. 2019).

Because magnetic fluctuations drift with the local Alfvén speed, it is important that we include a prescription for magnetic field amplification that is not only theoretically motivated, but consistent with observations. In our model, we implement a self-consistent prescription that incorporates the saturation points of both the resonant (Amato & Blasi 2006) and nonresonant (Bell 2004; Zacharegkas et al. 2019) streaming instabilities. This model yields magnetic fields that are consistent with those inferred from X-ray observations of young SNRs (Vink & Laming 2003; Völk et al. 2005; Parizot et al. 2006; Caprioli et al. 2008) and reproduces the observed relationship between shock velocity and downstream Alfvén speed reported in Zeng et al. (2019).

With this prescription for magnetic field amplification (also see Cristofari et al. 2021), our model produces modestly steep spectra $\propto E^{-2.34}$ for a Tycho-like SNR after 400 yr: $n_{ISM} = 1$ cm^{-3}, $B_0 = 3$ μG, $E_{SN} = 10^{51}$ erg, and $M_{ej} = 1$ $M_\odot$. We also confirm that the postcursor is the dominant source of this steepening; neglecting the effect of the precursor still yields spectra $\propto E^{-2.30}$.

As SNRs age and slow down, we find that this steepening diminishes, yielding a power-law slope, $q \simeq 2.23$ for our

prototypical SNR after 10^5 yr. Given observational constraints on the slope of the CR diffusion coefficient, this slope is consistent with that needed to reproduce the spectrum of Galactic CRs observed at Earth (e.g., Evoli et al. 2019, 2020).

More generally, for large v_{sh}, the nonresonant instability dominates magnetic field amplification such that the magnetic pressure scales as $v_{sh}P_{CR}$. As a result, the downstream Alfvén speed and thus the steepening due to the postcursor diminish as the SNR slows. This dependence largely disappears at lower v_{sh}, when the resonant instability dominates. The location of this transition, v_{sh}^*, depends on the ambient density and magnetic field (Equation (8)).

The relationship between v_{sh}, magnetic field amplification, and q that arises from postcursor physics provides a theoretically motivated explanation for the modestly steep spectra of Galactic SNRs ($\propto E^{-2.2}$), the very steep spectra of radio SNe ($\propto E^{-3}$), and the connection between them. More specifically, we use our formalism to model both source classes and find that we are able to produce spectra in good agreement with observations.

Our work represents the first generalization of postcursor physics to a wide range of SNR shocks, as well as the first self-consistent quantification of the spectral steepening that arises. The good agreement between our modeled spectra and those inferred from the nonthermal emission of real SNRs implies that the presence of a postcursor may resolve the tension between DSA predictions and observations.

Appendix
Solving the CR-modified Jump Conditions

We calculate the total compression ratio, R_{tot}, by solving the equations for conservation of mass, momentum, and energy across the shock in a manner similar to that described in Haggerty & Caprioli (2020). For a 1D, stationary shock, these equations read,

$$\rho(x)u(x) = \rho_0 u_0 \tag{A1}$$

$$\rho(x)u(x)^2 + P_g(x) + P_B(x) + P_{CR}(x) = \rho_0 u_0^2 + P_{g,0}, \text{ and} \tag{A2}$$

$$\frac{\rho(x)u^3(x)}{2} + F_g(x) + F_B(x) + F_{CR}(x) = \frac{\rho_0 u_0^3}{2} + F_{g,0} + F_{CR,0}, \tag{A3}$$

where F refers to the energy flux and subscripts g, B, and CR refer to the gas, magnetic field, and CR components, respectively. We take the contribution of the magnetic field to be negligible in the far upstream, since the amplified field is typically much larger than the interstellar one.

However, while Haggerty & Caprioli (2020) closes this system of equations by neglecting the CR escape flux, $F_{CR,0}$, we allow this flux to be nonzero. By using the canonical assumption that the CR distribution, $f(x, p)$, is continuous across the shock (i.e., that CRs have gyroradii large enough not

to see the shock jump), all of the moments of $f(x, p)$ are also continuous; this means that P_{CR} and F_{CR} are the same immediately upstream and downstream of the subshock. Thus, we solve Equation (A3) across the subshock rather than between downstream and upstream infinity, leaving $F_{CR,0}$ to be defined by the solution of the CR transport equation.

The gas and magnetic energy fluxes can be written as in Haggerty & Caprioli (2020),

$$F_g(x) = \frac{\gamma_g}{\gamma_g - 1} u(x) P_g(x), \text{ and} \tag{A4}$$

$$F_B(x) = (2\tilde{u}(x) + u(x)) P_B(x), \tag{A5}$$

where $\gamma_g = 5/3$ is the adiabatic index of the gas and $\tilde{u}(x)$ is the velocity of the magnetic fluctuations, $u(x) \pm v_A(x)$. Note that Equation (A5) assumes magnetic fluctuations are Alfvénic (Scholer & Belcher 1971; Vainio & Schlickeiser 1999; Caprioli et al. 2009a); while this is not strictly the case for turbulent fields, this prescription captures the fact that there are both Poynting and kinetic fluxes, and is empirically validated by kinetic simulations (Haggerty & Caprioli 2020). In the downstream, $\tilde{u}(x)$ becomes $u_2(1 + \sqrt{2R_{tot}\xi_{B,2}})$. For simplicity, we neglect the drift of magnetic fluctuations relative to the upstream flow, since $u_1 \gg v_{A,1}$.

Substituting Equations (A4) and (A5) into Equation (A3), dividing by $\rho_0 u_0^3/2$, and assuming a gaseous subshock, we obtain,

$$r^2 + \frac{\eta_g r^{-\gamma_g}}{\gamma_g M^2} + 6r\xi_{B,1} = \frac{1}{R_{tot}^2}$$
$$+ \frac{\eta_g \xi_{g,2}}{R_{tot}} + (6 + 4\sqrt{2R_{tot}\xi_{B,2}})\frac{\xi_{B,2}}{R_{tot}}, \tag{A6}$$

where $r \equiv R_{sub}/R_{tot}$ and $\eta_g \equiv 2\gamma_g/(\gamma_g - 1)$. Recall also that $\xi_i \equiv P_i/(\rho_0 u_0^2)$. In the strong shock limit ($M \gg 1$), the second term on the left-hand side can be neglected.

Assuming a strong shock, r and $\xi_{g,2}$ can be rewritten in terms of known quantities by solving Equation (A2), normalized to $\rho_0 u_0^2$, over the subshock and full shock, respectively:

$$r = 1 - \xi_{CR} - \xi_{B,1} \simeq 1 - \xi_{CR}, \text{ and} \tag{A7}$$

$$\xi_{g,2} = 1 - \frac{1}{R_{tot}} - \xi_{CR} - \xi_{B,2}. \tag{A8}$$

We relate $\xi_{B,1}$ and $\xi_{B,2}$ by assuming that the magnetic field is compressed downstream: $\xi_{B,2} = R_{sub}^2 \xi_{B,1}$.

Equations (A6)–(A8) can be combined into a single polynomial, written in terms of $x \equiv \sqrt{R_{tot}}$:

$$c_1 x^4 + c_2 x^3 + c_3 x^2 + c_4 = 0, \tag{A9}$$

where

$$c_1 = -(1 - \xi_{CR})^2,$$
$$c_2 = 2^{5/2}\xi_{B,2}^{3/2},$$
$$c_3 = \eta_g(1 - \xi_{CR} - \xi_{B,2}) + 6\xi_{B,2}, \text{ and}$$
$$c_4 = 1 - \eta_g + \frac{6\xi_{B,2}}{1 - \xi_{CR}}. \tag{A10}$$

Here, again we assume a strong shock for simplicity. We also write everything in terms of $\xi_{B,2}$, in keeping with Figures 2 and 7.

It is also possible to solve for R_{tot} in terms of $\xi_{B,1}$, but the resulting polynomial is substantially more complicated.

Equation (A9) has two positive roots, one of which corresponds to $1 \lesssim R_{tot} \lesssim 2$; the other corresponds to the physical solution used in the paper.

ORCID iDs

Rebecca Diesing ● https://orcid.org/0000-0002-6679-0012
Damiano Caprioli ● https://orcid.org/0000-0003-0939-8775

References

Acero, F., Ackermann, M., Ajello, M., et al. 2016, ApJS, 224, 8
Amato, E., & Blasi, P. 2005, MNRAS, 364, L76
Amato, E., & Blasi, P. 2006, MNRAS, 371, 1251
Amato, E., & Blasi, P. 2009, MNRAS, 392, 1591
AMS Collaboration, Aguilar, M., Cavasonza, A., et al. 2018, PhRvL, 120, 021101
Archambault, S., Archer, A., Benbow, W., et al. 2017, ApJ, 836, 23
Axford, W. I., Leer, E., & Skadron, G. 1977, in Int. Cosmic Ray Conf., 2, Acceleration of Cosmic Rays at Shock Fronts, 273
Bamba, A., Yamazaki, R., Yoshida, T., Terasawa, T., & Koyama, K. 2005, ApJ, 621, 793
Bell, A. R. 1978, MNRAS, 182, 147
Bell, A. R. 2004, MNRAS, 353, 550
Bell, A. R., Matthews, J. H., & Blundell, K. M. 2019, MNRAS, 488, 2466
Bell, A. R., Schure, K. M., & Reville, B. 2011, MNRAS, 418, 1208
Bell, A. R., Schure, K. M., Reville, B., & Giacinti, G. 2013, MNRAS, 431, 415
Berezhko, E. G., & Ellison, D. C. 1999, ApJ, 526, 385
Berezhko, E. G., & Völk, H. J. 1997, APh, 7, 183
Berezhko, E. G., & Völk, H. J. 2007, ApJL, 661, L175
Blandford, R., & Eichler, D. 1987, PhR, 154, 1
Blandford, R. D., & Ostriker, J. P. 1978, ApJL, 221, L29
Blasi, P. 2002, APh, 16, 429
Blasi, P. 2004, APh, 21, 45
Blasi, P., & Amato, E. 2012a, JCAP, 1, 10
Blasi, P., & Amato, E. 2012b, JCAP, 1, 11
Blasi, P., Amato, E., & Caprioli, D. 2007, MNRAS, 375, 1471
Blasi, P., Amato, E., & D'Angelo, M. 2015, PhRvL, 115, 121101
Blasi, P., Morlino, G., Bandiera, R., Amato, E., & Caprioli, D. 2012, ApJ, 755, 121
Bykov, A. M., Brandenburg, A., Malkov, M. A., & Osipov, S. M. 2013, SSRv, 178, 201
Caprioli, D. 2011, JCAP, 5, 26
Caprioli, D. 2012, JCAP, 7, 38
Caprioli, D., Amato, E., & Blasi, P. 2010a, APh, 33, 160
Caprioli, D., Amato, E., & Blasi, P. 2010b, APh, 33, 307
Caprioli, D., Blasi, P., & Amato, E. 2009a, MNRAS, 396, 2065
Caprioli, D., Blasi, P., Amato, E., & Vietri, M. 2008, ApJL, 679, L139
Caprioli, D., Blasi, P., Amato, E., & Vietri, M. 2009b, MNRAS, 395, 895
Caprioli, D., Haggerty, C. C., & Blasi, P. 2020, ApJ, 905, 2
Caprioli, D., Pop, A., & Spitkovsky, A. 2015, ApJL, 798, 28
Caprioli, D., & Spitkovsky, A. 2014a, ApJ, 794, 47
Caprioli, D., & Spitkovsky, A. 2014b, ApJ, 794, 46
Cardillo, M., Amato, E., & Blasi, P. 2015, APh, 69, 1
Cardillo, M., Amato, E., & Blasi, P. 2016, A&A, 595, A58
Chevalier, R. A. 1998, ApJ, 499, 810
Chevalier, R. A., & Fransson, C. 2006, ApJ, 651, 381
Chevalier, R. A., & Fransson, C. 2017, in Thermal and Non-thermal Emission from Circumstellar Interaction, ed. A. W. Alsabti & P. Murdin (Cham: Springer International Publishing), 875
Cristofari, P., Blasi, P., & Caprioli, D. 2021, A&A, 650, A62
Diesing, R., & Caprioli, D. 2018, PhRvL, 121, 091101
Diesing, R., & Caprioli, D. 2019, PhRvL, 123, 071101
Ellison, D. C., Baring, M. G., & Jones, F. C. 1996, ApJ, 473, 1029
Ellison, D. C., Berezhko, E. G., & Baring, M. G. 2000, ApJ, 540, 292
Ellison, D. C., & Reynolds, S. P. 1991, ApJ, 382, 242
Evoli, C., Aloisio, R., & Blasi, P. 2019, PhRvD, 99, 103023
Evoli, C., Morlino, G., Blasi, P., & Aloisio, R. 2020, PhRvD, 101, 023013
Fermi, E. 1954, Ap. J, 119, 1
Ghisellini, G. 2013, Radiative Processes in High Energy Astrophysics, Vol. 873 (Berlin: Springer)

Giordano, F., Naumann-Godo, M., Ballet, J., et al. 2012, ApJL, 744, L2
Green, D. A. 2019, JApA, 40, 36
Haggerty, C. C., & Caprioli, D. 2020, ApJ, 905, 1
Hanusch, A., Liseykina, T. V., Malkov, M., & Aharonian, F. 2019, ApJ, 885, 11
H.E.S.S. Collaboration, Abdalla, H., Abramowski, A., et al. 2018, A&A, 612, A6
Hillas, A. M. 2005, JPhG, 31, 95
Jones, F. C., & Ellison, D. C. 1991, SSRv, 58, 259
Kamble, A., Margutti, R., Soderberg, A. M., et al. 2016, ApJ, 818, 111
Kang, H., & Jones, T. W. 2005, ApJ, 620, 44
Kang, H., & Jones, T. W. 2006, APh, 25, 246
Kang, H., Jones, T. W., & Edmon, P. P. 2013, ApJ, 777, 25
Kang, H., & Ryu, D. 2018, ApJ, 856, 33
Kirk, J. G., Duffy, P., & Gallant, Y. A. 1996, A&A, 314, 1010
Krymskii, G. F. 1977, DoSSR, 234, 1306
Kulsrud, R., & Pearce, W. 1968, AJS, 73, 22
Lagage, P. O., & Cesarsky, C. J. 1983a, A&A, 118, 223
Lee, S.-H., Slane, P. O., Ellison, D. C., Nagataki, S., & Patnaude, D. J. 2013, ApJ, 767, 20
Malkov, M. A. 1997, ApJ, 485, 638
Malkov, M. A., & Aharonian, F. A. 2019, ApJ, 881, 2
Malkov, M. A., Diamond, P. H., & Sagdeev, R. Z. 2012, PhRvL, 108, 081104
Malkov, M. A., Diamond, P. H., & Völk, H. J. 2000, ApJL, 533, L171
Malkov, M. A., & O'C. Drury, L. 2001, RPPh, 64, 429
Margutti, R., Metzger, B. D., Chornock, R., et al. 2019, ApJ, 872, 18
Morlino, G., Amato, E., Blasi, P., & Caprioli, D. 2010, MNRAS, 405, L21
Morlino, G., Bandiera, R., Blasi, P., & Amato, E. 2012, ApJ, 760, 137
Morlino, G., & Blasi, P. 2016, A&A, 589, A7
Morlino, G., Blasi, P., Bandiera, R., Amato, E., & Caprioli, D. 2013, ApJ, 768, 148
Morlino, G., & Caprioli, D. 2012, A&A, 538, A81
O'C. Drury, L. 1983, RPPh, 46, 973
O'C. Drury, L., & Völk, H. J. 1981, ApJ, 248, 344
Parizot, E., Marcowith, A., Ballet, J., Gallant, Y. A., et al. 2006, A&A, 453, 387
Ptuskin, V., Zirakashvili, V., & Seo, E.-S. 2010, ApJ, 718, 31
Ressler, S. M., et al. 2014, ApJ, 790, 85
Saha, L., Ergin, T., Majumdar, P., Bozkurt, M., & Ercan, E. N. 2014, A&A, 563, A88
Scholer, M., & Belcher, J. W. 1971, SoPh, 16, 472
Skilling, J. 1975a, MNRAS, 172, 557
Skilling, J. 1975b, MNRAS, 173, 245
Skilling, J. 1975c, MNRAS, 173, 255
Slane, P., Lee, S.-H., Ellison, D. C., et al. 2014, ApJ, 783, 33
Soderberg, A. M., Brunthaler, A., Nakar, E., Chevalier, R. A., & Bietenholz, M. F. 2010, ApJ, 725, 922
Soderberg, A. M., Margutti, R., Zauderer, B. A., et al. 2012, ApJ, 752, 78
Tatischeff, V. 2009, A&A, 499, 191
Tran, A., Williams, B. J., Petre, R., Ressler, S. M., & Reynolds, S. P. 2015, ApJ, 812, 101
Truelove, J. K., & Mc Kee, C. F. 1999, ApJS, 120, 299
Vainio, R., & Schlickeiser, R. 1999, A&A, 343, 303
Vink, J., & Laming, J. M. 2003, ApJ, 584, 758
Vladimirov, A., Ellison, D. C., & Bykov, A. 2006, ApJ, 652, 1246
Völk, H. J., Berezhko, E. G., & Ksenofontov, L. T. 2005, A&A, 433, 229
Zacharegkas, G., Caprioli, D., & Haggerty, C. 2019, in Int. Cosmic Ray Conf., 36, 36th Int. Cosmic Ray Conf. (ICRC2019)
Zeng, H., Xin, Y., & Liu, S. 2019, ApJ, 874, 50
Zirakashvili, V. N., & Ptuskin, V. S. 2008, in AIP Conf. Proc. 1085, High Energy Gamma-Ray Astronomy, ed. F. A. Aharonian, W. Hofmann, & F. Rieger (Melville, NY: AIP), 336
Zweibel, E. G. 1979, in AIP Conf. Ser., 56, Particle Acceleration Mechanisms in Astrophysics, ed. J. Arons, C. McKee, & C. Max (Melville, NY: AIP), 319